Mechanically Tunable Optical Response in Silicon Nanosphere Metasurface Fabricated via Bottom-Up Process

Hu, Yongan
Probst, Patrick T.
Habil, Mojtaba Karimi
Sugimoto, Hiroshi
Fujii, Minoru

(Citation)
Advanced Optical Materials,Early View:01013

(Issue Date)
2025-06-26

(Resource Type)
journal article

(Version)
Version of Record

RESEARCH ARTICLE

ADVANCED OPTICAL MATERIALS
www.advopticalmat.de

Mechanically Tunable Optical Response in Silicon Nanosphere Metasurface Fabricated via Bottom-Up Process

Yongan Hu, Patrick T. Probst, Mojtaba Karimi Habil, Hiroshi Sugimoto, and Minoru Fujii**

Applications based on metasurfaces are often hampered by the limited scalability and real-time tunability of lithographically produced samples (top-down). Bottom-up approaches that start from nanoparticle building blocks relax these constraints. Here, a large-area mechano-tunable metasurface composed of a square array of silicon nanospheres (Si NSs) is introduced. The metasurface is produced by capillarity-assisted self-assembly of size-purified colloidal Si NSs that have Mie resonances in the visible and near-infrared range. The collective response of Si NSs in the metasurface exhibits reflectance peaks originating from electric (ED) and magnetic dipole (MD) resonances of individual Si NSs. The resonance wavelengths are sensitive to the lattice constant and thus can be modulated in a wide wavelength range (≈130 nm) by external mechanical strain. At a proper strain level, the ED and MD lattice resonances spectrally overlap, resulting in destructive interference of the backward scattering light (lattice Kerker effect), which strongly suppresses the reflectance. The reflectance modulation is at a maximum of 45.9% and is reversible over 100 stretching-releasing cycles. This suggests that the produced flexible metasurface can be a mechano-tunable flexible optical component.

1. Introduction

In a 2D array of nanoparticles, the coupling between diffracted waves and single-particle optical resonances modifies the resonance wavelength and reduces the bandwidth.[1–7] This phenomenon is called collective lattice resonance (CLR) and has been utilized for optical sensing,[8–11] structural coloration,[12–17] lasers,[18–21] etc. Metasurfaces with CLRs have usually been produced via top-down nanofabrication technology including electron beam lithography,[22–26] which guarantees accurate production of complicated structures. However, this method oftentimes suffers from small throughput, high cost, limited device size, and substrates limitations to rigid materials. In contrast, bottom-up assembly of nanoparticle nanoantennas—synthesized wet-chemically in large batches—into large-area CLR metasurfaces can help relax these constraints. Capillarity-assisted particle assembly (CAPA)[27–29] has been successfully employed to fabricate large-area metasurfaces for surface-enhanced Raman scattering,[30–32] biosensing[33–35] and light emitting devices.[36] CAPA accepts a wide range of colloidal materials (metal(oxides), semiconductors, polymers, biomolecules)[28] and substrates, including elastomers. This enables the convenient fabrication of mechano-tunable metasurfaces without the need for additional steps to transfer the nanoparticle array from the wafer to the elastic substrate, as is the case for lithographic approaches.[37–41] For example, modifying the lattice period of a bottom-up fabricated metasurface in situ via mechanical strain was demonstrated to produce a 70 nm spectral shift in a square lattice of gold nanoparticles on a dimethylpolysiloxane (PDMS) substrate.[42]

Previous studies on mechano-tunable metasurfaces focused on gold and silver nanoparticles that feature localized surface plasmon resonances.[43–46] Nonetheless, constructing active metasurfaces from high-refractive-index dielectrics instead, significantly improves metasurface performance and introduces additional degrees of freedom for spectral engineering. Compared to their plasmonic counterpart, high-refractive-index dielectric Mie resonators benefit from sharper resonances (reduced optical loss) and offer magnetic-type resonances in addition to electric-type ones. Their low-order Mie resonances are located in the visible to the near-infrared range,[47–51] and high-order multipolar modes can be excited easily.[52–54] The existence of two types of resonances with different radiation patterns enables us to design a CLR metasurface with a variety of functionalities.[55–60] For example, in a static 2D periodic array, one can control the resonance wavelengths of the electric dipole (ED) and magnetic dipole (MD) modes to make these two modes overlap by appropriately designing the lattice constants in the two orthogonal directions[56]

Y. Hu, P. T. Probst, M. K. Habil, H. Sugimoto, M. Fujii
Department of Electrical and Electronic Engineering
Graduate School of Engineering
Kobe University
1-1 Rokkodai, Nada, Kobe 657–8501, Japan
E-mail: sugimoto@eedept.kobe-u.ac.jp; fujii@eedept.kobe-u.ac.jp

The ORCID identification number(s) for the author(s) of this article can be found under https://doi.org/10.1002/adom.202501013

DOI: 10.1002/adom.202501013

or by tuning the incidence angle.[57] This overlap results in the so-called lattice Kerker effect where the reflectance is strongly suppressed due to destructive interference of the two modes. Introducing real-time tunability via mechanical strain in active dielectric metasurfaces would allow for (I) convenient post-fabrication adjustment of the operating window as well as (II) active control of reflectance and transmittance by reversibly switching on and off the lattice Kerker effect. Although theoretical considerations are available, the realization of dielectric CLR metasurfaces to actively control the lattice Kerker effect is still in its infancy.

In this work, we demonstrate the successful fabrication of a large-area 2D square array (≈0.7 cm × 1 cm) of silicon nanospheres (Si NSs) that enables real-time control of the lattice Kerker effect. To this end, we employ CAPA of colloidal, size-purified Si NSs on elastic PDMS substrates. We start with a numerical simulation of the reflectance spectra and study the condition to achieve the lattice Kerker effect by changing the lattice constants of two orthogonal directions. We then produce square lattice arrays that operate in the visible and near-infrared range depending on the Si NSs size and study their reflectance spectra under tensile strain. The ED and MD lattice resonance wavelengths are successfully modulated by the applied strain and the overlap of these two modes results in the disappearance of the reflectance peak.

2. Results and Discussion

2.1. Reflectance Spectra of a Si NS Square Array in a Dielectric Medium

Figure 1a shows a model structure of a Si NS square array embedded in a dielectric medium (n_m = 1.4). The diameter of a Si NS is 254 nm. The 2D array is illuminated from the normal to the surface by an *x*-polarized plane wave. Figure 1b shows the contour plot of the reflectance spectra when the lattice constant in the *y* direction (P*y*) is changed from 550 to 700 nm. The lattice constant in the *x*-direction is fixed at 550 nm. The Rayleigh anomalies RA*x* and RA*y* corresponding to the diffraction order (± 1, 0) and (0, ±1), respectively, are indicated with white dotted lines. To provide a better visualization of the different mode contributions, the reflectance spectra are plotted for some specific P*y* in Figure 1c. In a square lattice (P*x* = P*y* = 550 nm), reflectance peaks appear at 854 and 945 nm. These resonances originate from the ED and MD modes of individual Si NSs, which intrinsically resonate at the wavelength of 778 and 963 nm in a medium with a refractive index of 1.4 (Figure S3, Supporting Information). However, these resonances are shifted due to the inter-particle coupling within the periodic array and thus referred to as electric dipole lattice resonance (ED-LR) and magnetic dipole lattice resonance (MD-LR), respectively. The ED-LR peak shifts progressively to longer wavelengths with increasing P*y*, while the MD-LR is almost independent of P*y*. This behavior results in an overlap of ED-LR and MD-LR peaks around P*y* = 640 nm. This scenario satisfies the lattice Kerker condition and the reflectance is strongly suppressed because far-field radiation from the ED-LR and MD-LR cancel out each other. Further increase of P*y* results in the reappearance of the ED-LR and MD-LR peaks.

To further investigate the near-field interactions of Si NSs, we visualize the magnitude (color bar) and direction (white arrows) of the electric field for both the square lattice structure and the deformed lattice structure under the lattice Kerker condition (P*x* = 550 nm and P*y* = 640 nm) in Figure 1d,e, respectively. For the square lattice structure at the MD-LR resonance wavelength of 945 nm, the electric field forms a loop around the *y*-axis, concentrated inside and around the perimeter of the Si NSs (Figure 1d, top panel). This distribution is the characteristic of an MD emitter and confirms the excitation of the MD mode in Si NSs. At the ED-LR resonance wavelength of 854 nm, the electric field arrows form a characteristic dipolar pattern, with strong electric field lobes extending outward from the Si NSs along the polarization direction of the incident field (Figure 1d, bottom panel). This pattern matches the field distribution of a dipolar emitter and confirms the excitation of the ED mode in Si NSs. Under the lattice Kerker condition (Figure 1e), both the circulating electric field and the localized field concentration at the poles of the Si NSs are present, which further verify the near-field coupling and the overlap of the ED and MD modes.

Figure 1f shows the contour plot of the reflectance when P*x* is changed from 550 to 700 nm at fixed P*y* (550 nm), and Figure 1g highlights representative spectra thereof at some specific P*x*. In this case, MD-LR shifts to longer wavelengths, while the ED-LR wavelength remains almost constant. Therefore, modulation of the lattice constant in the *x*-direction cannot produce the lattice Kerker effect, as no spectral overlap of ED-LR and MD-LR can be achieved.

2.2. Bottom-Up Fabrication of Si NSs Square Lattice Array

We fabricate a Si NSs square lattice array by CAPA using a colloidal suspension of size-purified Si NSs developed in our group as a starting material. Their narrow size and shape distributions are crucial to ensure sharp resonances and strong inter-particle coupling in the final CLR metasurface, as has been demonstrated for plasmonic nanoparticles.[42] This high structural quality of the array is an important prerequisite for achieving a distinct lattice Kerker effect. **Figure 2a** depicts the fabrication of size-selected Si NSs in a colloidal suspension schematically. Details of the procedure are shown in our previous paper[61] and in the Experimental section. Briefly, Si NSs are grown in silicon dioxide matrices by the thermal disproportionation reaction of silicon monoxide (SiO) powder, and then Si NSs are extracted in solution by hydrofluoric etching of the matrices. Subsequently, the Si NS suspension is size-separated by a density gradient centrifugation process. Figure 2b shows a photo of methanol suspensions containing Si NSs of different sizes. The average diameter (D_{ave}) is indicated below the photo. The colors arise from size-dependent Mie scattering of the Si NSs. The transmission electron microscope (TEM) images in Figure 2c highlight the quality of the Si NSs characterized by distinct circularity and high crystallinity. In the high-resolution image on the right, the lattice fringe corresponds to {111} planes. Figure 2d shows the extinction spectrum of a colloidal suspension (D_{ave} = 254 nm) together with a calculated spectrum that takes into account the size distribution (standard deviation divided by the average diameter (CV, coefficient of variation) is 10%). The measured and calculated spectra coincide

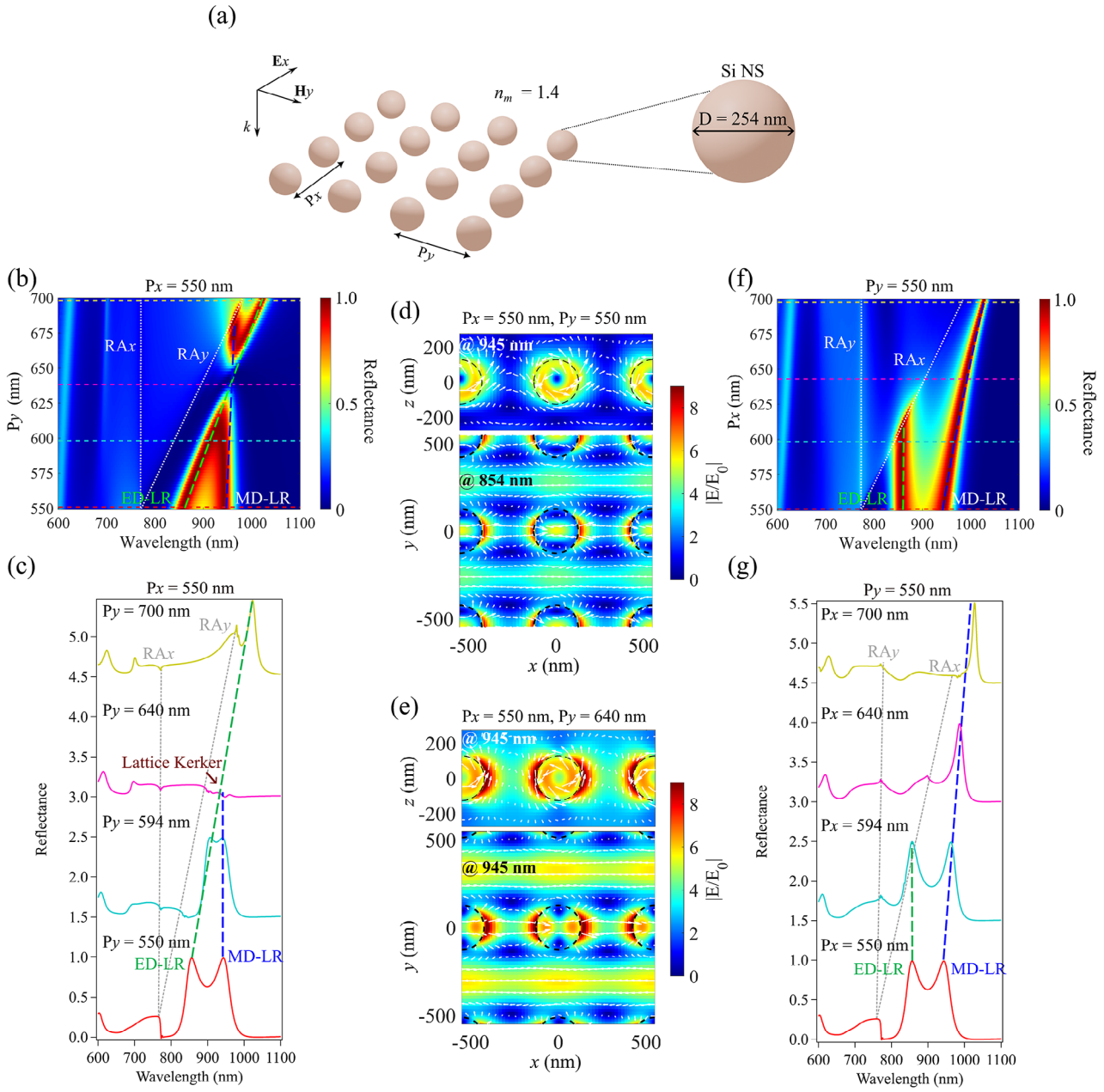

Figure 1. a) Model structure of a Si NS 2D array for numerical simulations. The diameter of Si NSs is 254 nm. P*x* and P*y* represent the pitches in the *x* and *y* directions, respectively. NSs are embedded in a dielectric medium with a refractive index of 1.4. The NS array is illuminated from the top by a plane wave polarized in the *x*-direction. b) Contour plot of reflectance spectra. P*x* is fixed to 550 nm, while P*y* is varied from 550 to 700 nm. The peak positions of the ED-LR and the MD-LR are indicated by green and blue dashed lines, respectively. The Rayleigh anomalies (RA*x* and RA*y*) are pointed out by white dotted lines. c) Reflectance spectra at some specific P*y*'s. P*x* is fixed to 550 nm. d, e) Contour plots of the electric field enhancement factors in the *x*-*z* (upper panel) and *x*-*y* planes (bottom image) for (d) P*x* = P*y* = 550 nm at the wavelength of 945 nm (upper) and 854 nm (bottom), and (e) P*x* = 550 nm and P*y* = 640 nm at the wavelength of 945 nm. f) Contour plot of the reflectance spectra. P*x* varies from 550 to 700 nm, while P*y* is fixed to 550 nm. The peak positions of the ED-LR and the MD-LR are indicated by green and blue dashed lines, respectively, and the Rayleigh anomalies (RA*x* and RA*y*) are pointed out by white dotted lines. g) Reflectance spectra at some specific P*x*'s. P*y* is fixed to 550 nm.

well, indicating the high quality of the colloidal suspension with a small size distribution.

Figure 2e shows the procedure to produce a Si NSs square array from the Si NSs suspension by CAPA (see Section S2, Supporting Information for details). We use a square lattice hole array made on PDMS as a template (see Section S1, Supporting Information for template preparation). The hole diameter is 300 nm, and the pitch is 550 nm. The area of the template is ≈1 cm × 0.7 cm. To fill the holes with Si NSs, a droplet of Si NSs suspension (30 µL, 0.8 mg ml^{-1}) is applied on the template and dragged across the nanopatterned area by a guiding glass (see Experimental section for details). Due to the

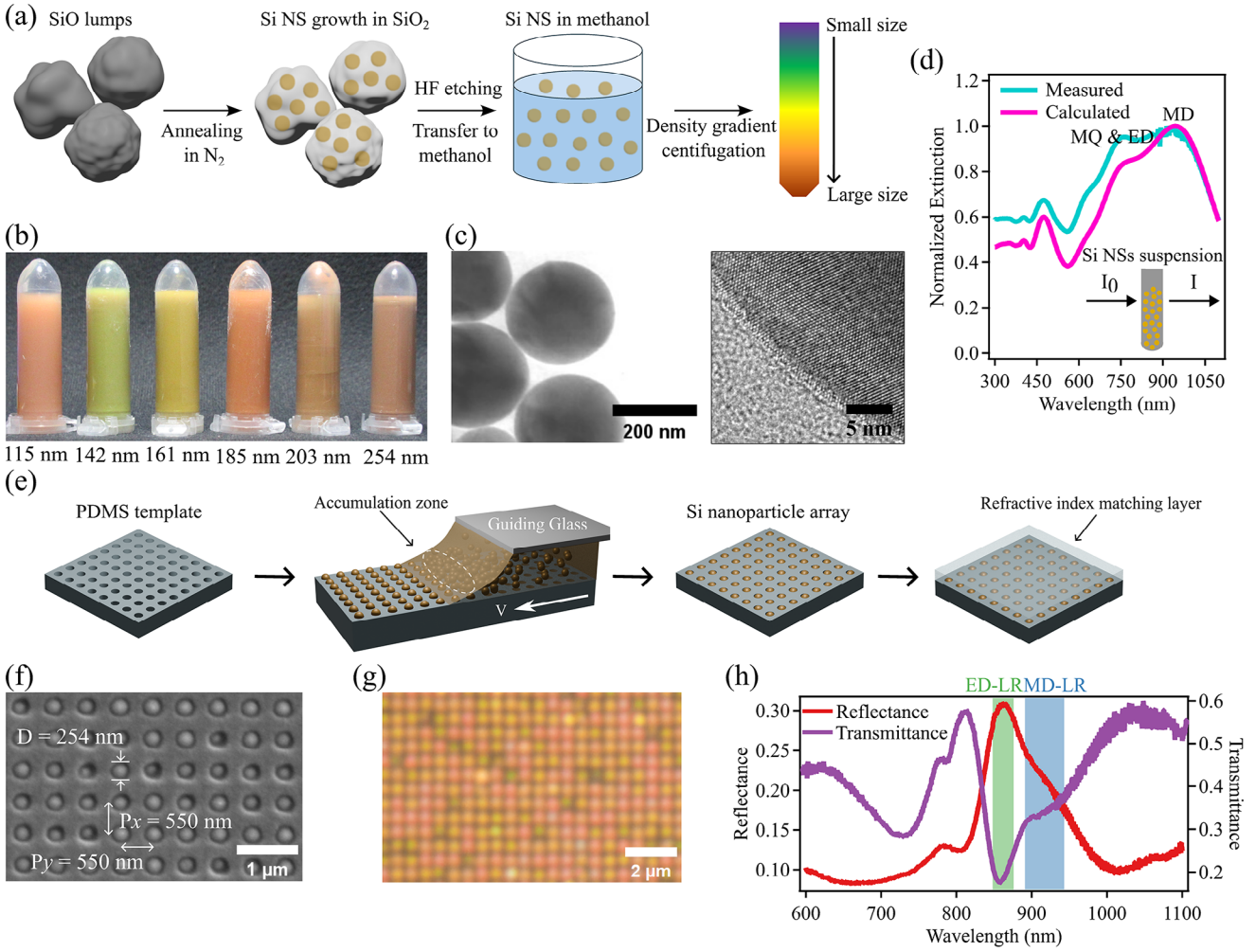

Figure 2. a) Synthesis procedure of size-selected Si NSs. b) Photos of Si NSs suspensions. The average diameter of Si NSs is shown below the photo. c) TEM and high-resolution TEM images of Si NSs. d) Extinction spectrum of a suspension of Si NSs with the average diameter of 254 nm (blue), and calculated extinction spectrum of Si NSs obtained by taking into account the size distribution (pink). e) Fabrication procedure of Si NSs 2D array. f) SEM image of a Si NSs 2D array. g) Optical microscope image of a Si NSs 2D array. h) Reflectance and transmittance spectra of the Si NSs 2D array in (f) and (g). The ED-LR and MD-LR regions are indicated by green and blue shades, respectively.

evaporation of the liquid, the nanoparticles accumulate at the liquid meniscus and are deposited inside the nanoholes by capillary forces. After filling the holes with Si NSs and drying, a PDMS refractive index matching layer (≈1 mm in thickness) is deposited on top.

Figure 2f and Figure S4b (Supporting Information) show scanning electron microscope (SEM) images of a Si NSs-filled square lattice array (D_{ave} = 254 nm). Evaluating ten 10 × 7 μm-sized SEM images reveals that on average 95.9% of the holes are filled with single Si NSs, 3.3% are filled by Si NSs dimers, 0.2% are filled by Si NSs trimers and 0.5% are empty. The bright-field microscopy image in Figure 2g shows light scattered by the individual Si NSs in the densely filled 2D array (see Figure S4a, Supporting Information for a larger size image). The individual colors are mostly pinkish, but greenish and yellowish spots are also present because the Mie scattering is sensitive to small size variations of the Si NSs.

Figure 2h shows the reflectance and transmittance spectra of the Si NSs 2D array under illumination with unpolarized light from a halogen lamp. From the comparison with numerical simulations, in the reflectance spectrum, the peak ≈864 nm is assigned to the ED-LR, and the broad shoulder ≈900 nm to the MD-LR. The experimentally observed reflectance spectrum is broader than that of the calculated one in Figure 1 and the intensity is lower. This may arise from inhomogeneities in the actual sample such as the size distribution of Si NSs and the imperfection of the lattice structure. It should be noted that the sample is rather uniform and the variation of the peak reflectance is less than 5% at different positions within a sample (see Figure S5, Supporting Information).

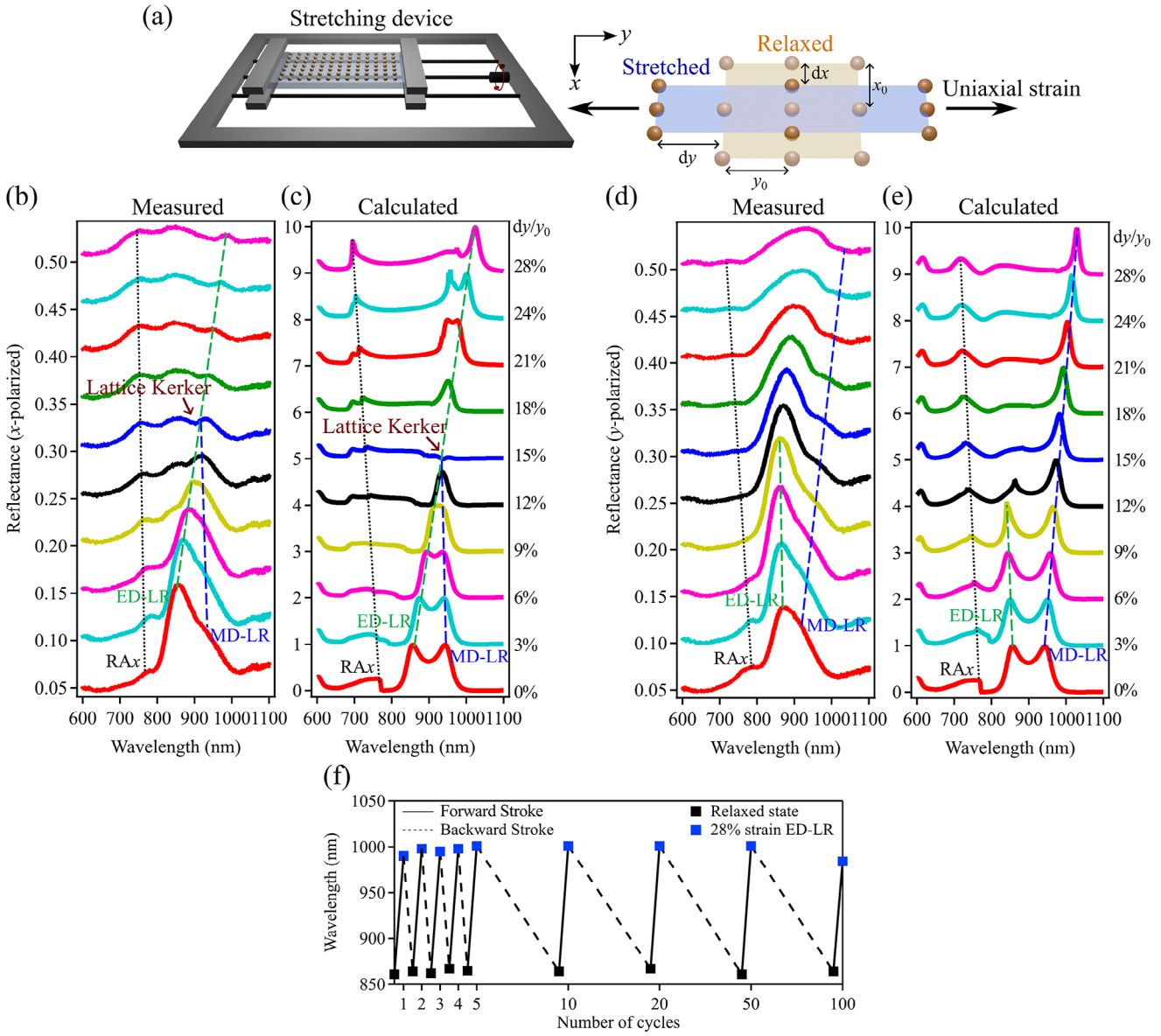

Figure 3. a) Schematic illustration of the uniaxial stretching device employed to measure strain-induced reflectance modulation, including definitions of the coordinate system and relevant lattice parameters. A Si NSs 2D array is stretched along the *y*-direction. b,c) Measured (b) and calculated (c) reflectance spectra under *x*-polarized incidence. The strain (dy/y_0) is changed from 0 to 28%. The green and blue dashed lines indicate peaks of the ED-LR and MD-LR, respectively. The black dot lines show the RA*x*. d,e) Measured (d) and calculated (e) reflectance spectra under *y*-polarized incidence. The strain (dy/y_0) is changed from 0 to 28%. f) ED-LR wavelength under *x*-polarized light illumination as a function of stretching-releasing cycles. The strain is changed between $dy/y_0 = 0$ and 28.

2.3. Strain-Controlled Lattice Kerker Effect

We fixed a PDMS film featuring a Si NSs square lattice array in a stretching device, as schematically shown in **Figure** 3a, and measured the reflectance spectra under uniaxial strain in the *y*-direction. The uniaxial strain expands the film in the *y*-direction and shrinks it in the *x*-direction (Poisson ratio = 0.38, see Section S6, Supporting Information). Figure 3b shows the reflectance spectra measured under *x*-polarized light illumination. The maximum strain (dy/y_0) is 28%. With increasing strain, the ED-LR shifts from 864 to 998 nm (green dashed line), while the MD-LR wavelength is almost constant (blue dashed line). This is due to strain-induced tuning of the lattice constants in the 2D array, in accordance with Figure 1 which describes the change in reflectance depending on the lattice constant. As a result, the ED-LR and the MD-LR overlap at $dy/y_0 = 15\%$, and the reflectance is strongly suppressed, i.e., the lattice Kerker effect arises. Figure 3b demonstrates that mechanical strain is a reliable means to modulate the reflectance of a dielectric CLR metasurface on an elastic foundation and can induce the lattice Kerker effect.

In Figure 3c, calculated reflectance spectra that take into account the experimentally observed Poisson ratio of 0.38 are

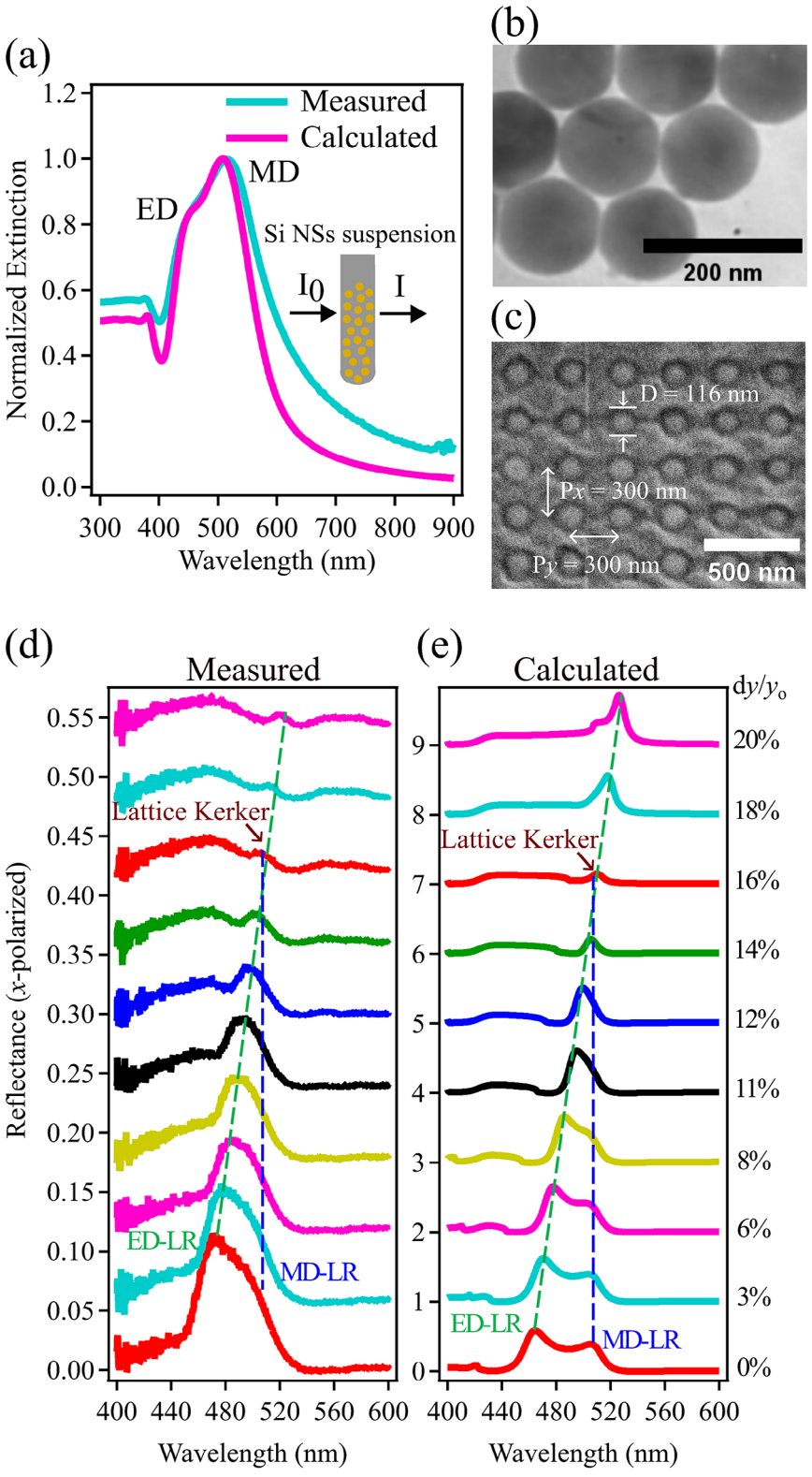

Figure 4. a) Extinction spectrum of a suspension of Si NSs with the average diameter of 116 nm (blue), and calculated extinction spectrum of Si NSs obtained by taking into account the size distribution (CV = 11%) (pink). b) TEM image of Si NSs in the suspension in (a). c) SEM image of a Si NSs 2D square array produced from the suspension in (a). d,e) Measured (d) and calculated (e) reflectance spectra under *x*-polarized incidence. The strain (dy/y_0) is changed from 0 to 20%. The green and blue dashed lines indicate peaks of the ED-LR and MD-LR, respectively.

shown. The overall change of the spectral shape by strain is similar to that in Figure 3b, and the lattice Kerker effect appears at $d\gamma/\gamma_0 = 15\%$. However, there are some discrepancies. First, the experimental spectra are broader than the calculated ones. This may be due to the size distribution of Si NSs and the imperfection of the lattice structure in the actual sample, which is not considered in the simulation. Another discrepancy is the different spectral shape after crossing the lattice Kerker condition. In the calculation, the intensity of the ED-LR reflection recovers, while it remains very weak in the experiment. The reason for the difference is not very clear, but it may arise from some inhomogeneities induced in the actual sample under strong strain.

Figure 3d,e show the measured and calculated reflectance spectra, respectively, when the incident light is polarized in the *y*-direction. In this case, the MD-LR shifts to longer wavelengths, while the ED-LR wavelength is almost independent of the strain. Therefore, the lattice Kerker effect does not occur.

The change of the reflectance spectra by strain in Figure 3b,d is reversible. In Figure 3f, the reflectance peak wavelengths under *x*-polarized light illumination at $d\gamma/\gamma_0 = 0$ and 28% of strain are plotted as a function of the stretching-releasing cycles up to 100 times. The ED-LR peak wavelength shifts reversibly by 15.5%, between 864 ± 3 nm (relaxed state) and 998 ± 14 nm. At the same time, reflectivity at 864 nm is modulated by 45.9%. This dynamic and fully reversible spectral tuning opens up possibilities to control reflectivity in real-time and enables the design of active nano-optical components to further push device miniaturization.

An additional advantage of Mie-resonant metasurface building blocks like Si NSs compared to plasmonic nanoparticles is the large spectral range accessible by controlling the nanoparticle size.[61] In Figure 3, the square lattice array is produced from Si NSs with an average diameter of 254 nm, having the lowest order Mie resonances ≈900 nm. By reducing the size, the resonance wavelength, and thus the reflectance peaks of the metasurface, can be brought to the visible range. In order to demonstrate this, we produce a square lattice array of Si NSs with an average diameter of 116 nm. **Figure** 4a shows the measured and calculated extinction spectra of the colloidal suspension. The MD resonance is ≈516 nm, while the ED is visible as a shoulder ≈450 nm. A TEM image of the Si NSs is shown in Figure 4b. These Si NSs are selectively deposited inside the nanoholes of the 2D periodic template (hole diameter 145 nm, pitch 300 nm), as confirmed by scanning electron microscopy (Figure 4c).

Figures 4d and e show the measured and calculated reflectance spectra of the 2D array under *x*-polarized illumination at various strains. Strain-induced shift and overlap of ED-LR and MD-LR produce the lattice Kerker effect at a strain ($d\gamma/\gamma_0$) of 16%, which results in a strong reduction of the reflectance. Consequently, for the 116 nm sized Si NSs, the reflectance is strongly modulated ≈500 nm, as compared to the operation window ≈900 nm in the case of the 254 nm Si NSs (Figure 3). This highlights the versatility of mechano-tunable CLR metasurfaces constructed from colloidal nanoparticles. The utilization of other high-refractive-index dielectric materials could further extend the accessible wavelength range in the future. In the case of *y*-polarization incidence, the lattice Kerker effect does not occur as in the case of Figure 3d (Figure S7, Supporting Information).

3. Conclusion

We realized mechano-tunable CLR metasurfaces comprising dielectric nanoparticles to actively control reflectance in the visible and near-infrared range. Capillarity-assisted particle assembly of Si NSs into 2D periodic arrays facilitated the seamless integration of the metasurface into an elastic substrate, which is typically challenging for lithographic methods. The high filling rate (> 90%) and well-defined optical properties of the size-purified nanoparticles ensured strong inter-particle coupling. Consequently, collective lattice resonances (ED-LR, MD-LR) were excited. Applying tensile strain to the samples modified the lattice constants and thereby reversibly shifted the ED-LR by up to 134 nm. When ED-LR and MD-LR were made to overlap spectrally, the reflectance was strongly reduced (modulation depth = 45.9%) due to the induced lattice Kerker effect. The introduced approach provides a blueprint for the design and fabrication of active nano-optical components and its generalization to other high-index dielectric materials can further widen the operating frequencies.

4. Experimental Section

Preparation of the Colloidal Suspension of Si NSs: Si NSs were prepared by thermal disproportionation of silicon monoxide (SiO). SiO lumps (several mm in size) (99.9%, FUJIFILM Wako) were crushed to powder and annealed at 1475 °C in a nitrogen gas atmosphere for 30 min to grow crystalline Si NSs in silica matrices. Etching out silica matrices in a hydrofluoric acid solution (HF, 48 wt.%) for 1 h resulted in the extraction of freestanding Si NSs. HF was then removed by a centrifugation process, and Si NSs were transferred into methanol and sonicated in an ultrasonic homogenizer (SONICSTAR 85, Violamo) for a minute. Finally, Si NSs were transferred to surfactant by centrifugation processes.

Capillarity-Assisted Particle-Assembly of Si NSs: A custom-built setup was used for the CAPA. In the case of Si NSs with 254 nm average diameter, 30 µL nanoparticle suspension [0.8 mg mL^{-1} Si NSs, 1 mM sodium dodecyl sulfate, 0.1 wt.% Triton X-45 (Sigma-Aldrich)] was confined between the template and the stationary glass slide (gap ≈ 500 µm), and the patterned substrate was withdrawn underneath the droplet at a speed of 1 µm s^{-1} by a motorized translational stage (SGSP20-35 controlled by a Mark-202, SIGMA KOKI). The temperature of the stage was set to 15–20 K above the dew point (temperature controller TR-KN-T, AS ONE). For the assembly of 116 nm-sized Si NSs, the nanoparticle concentration was adjusted to 0.1 mg $ml^{-1,}$ and the temperature of the stage was set to 30 K above the dew point. Further experimental details can be found in Section S2 (Supporting Information).

Structural Characterization: For TEM and SEM observations JEM-2100F (JEOL) and JSM-IT800 (JEOL), respectively, were used.

Reflectance Measurement: A custom-built inverted optical microscope was used for reflectance measurements. Samples were illuminated by a halogen lamp via an objective lens (10 ×, NA = 0.3), and reflected light was collected by the same objective lens, transferred to the entrance slit of a monochromator (Kymera 328i, Andor), and detected by a cooled CCD (Newton, Andor). The size of the measurement area on a sample was 286 µm × 200 µm.

Numerical Simulation: The reflectance spectra and field distributions of metasurfaces were calculated using the finite-difference time-domain (FDTD) method utilizing commercial software (Lumerical, Ansys). A unit cell of the structure illuminated by a linearly polarized plane wave in the *x*/*y*-direction propagating normally to the lattice surface (*z*-direction). The periodic boundary conditions were applied along the *x*-*z* and *y*-*z* planes, while a perfectly matched layer was implemented in the *z*-direction to minimize artificial reflections from the domain boundaries. The reflectance

spectra were extracted by 2D power monitors normal to the *z* axis. To ensure the numerical convergence a uniform mesh size 20 nm in all directions was employed with a finer mesh 8 nm in the Si NSs domain. The refractive index of Si NSs was taken from Palik[62] while the background refractive index was set to 1.4 (PDMS).

Supporting Information

Supporting Information is available from the Wiley Online Library or from the author.

Acknowledgements

This work is partially supported by the JSPS KAKENHI 22K18949, 23K21065, 24KF0158, 24K01287, 24H00400, and 25K01608. P.T.P. was supported by a "JSPS Postdoctoral Fellowship for Research in Japan". M.K.H. is supported by a "JSPS Postdoctoral Fellowship for Research in Japan".

Conflict of Interest

The authors declare no conflict of interest.

Data Availability Statement

The data that support the findings of this study are available from the corresponding author upon reasonable request.

Keywords

all-dielectric tunable metasurface, capillarity-assisted particle-assembly, flexible metasurface, lattice Kerker effect, Mie resonance, silicon nanoparticle

Received: March 30, 2025
Revised: May 22, 2025
Published online:

[1] S. Baur, S. Sanders, A. Manjavacas, *ACS Nano* **2018**, *12*, 1618.
[2] A. D. Utyushev, V. I. Zakomirnyi, I. L. Rasskazov, *Rev. Phys.* **2021**, *6*, 100051.
[3] G. W. Castellanos, P. Bai, J. G. Rivas, *J. Appl. Phys.* **2019**, *125*, 213105.
[4] W. Wang, M. Ramezani, A. I. Väkeväinen, P. Törmä, J. G. Rivas, T. W. Odom, *Mater. Today* **2018**, *21*, 303.
[5] K. Yang, X. Yao, B. Liu, B. Ren, *Adv. Mater.* **2021**, *33*, https://doi.org/10.1002/adma.202007988.
[6] B. Wang, P. Yu, W. Wang, X. Zhang, H. C. Kuo, H. Xu, Z. M. Wang, *Adv. Opt. Mater.* **2021**, *9*, https://doi.org/10.1002/adom.202001520.
[7] K. Imaeda, J. Yue, H. Takeuchi, K. Ueno, *J. Phys. Chem. C* **2024**, *128*, 5659.
[8] N. Liu, M. Mesch, T. Weiss, M. Hentschel, H. Giessen, *Nano Lett.* **2010**, *10*, 2342.
[9] X. Wen, S. Deng, *Adv. Opt. Mater.* **2023**, *11*, https://doi.org/10.1002/adom.202300401.
[10] R. Guo, L. Chen, Z. Yan, R. Ma, S. Feng, S. Deng, *J. Phys. Chem. C* **2024**, *128*, 11298.
[11] E. Csányi, Y. Liu, D. Kai, S. Sugiarto, H. Y. Loong Lee, F. Tjiptoharsono, Q. Ruan, S. Daqiqeh Rezaei, X. Chi, A. Rusydi, G. Leggett, J. K. W. Yang, Z. Dong, *Nano Lett.* **2025**, *25*, 3906.
[12] M. Song, D. Wang, S. Peana, S. Choudhury, P. Nyga, Z. A. Kudyshev, H. Yu, A. Boltasseva, V. M. Shalaev, A. V. Kildishev, *Appl. Phys. Rev.* **2019**, *6*, 041308.
[13] F. Gildas, Y. Dan, *J. Nanophotonics* **2019**, *13*, https://doi.org/10.1117/1.JNP.13.020901.
[14] S. Daqiqeh Rezaei, Z. Dong, J. You En Chan, J. Trisno, R. J. H. Ng, Q. Ruan, C. W. Qiu, N. A. Mortensen, J. K. W. Yang, *ACS Photonics* **2021**, *8*, 18.
[15] X. Zhu, C. Vannahme, E. Højlund-Nielsen, N. A. Mortensen, A. Kristensen, *Nat. Nanotechnol.* **2016**, *11*, 325.
[16] F. Cheng, J. Gao, S. T. Luk, X. Yang, *Sci. Rep.* **2015**, *5*, https://doi.org/10.1038/srep11045.
[17] Y. Sugimoto, K. Kajikawa, D. Mayer, A. Offenhäusser, M. Toma, A. C. S. Appl, *Nano Mater* **2024**, *7*, 26423.
[18] F. Freire-Fernández, J. Cuerda, K. S. Daskalakis, S. Perumbilavil, J. P. Martikainen, K. Arjas, P. Törmä, S. van Dijken, *Nat. Photonics* **2022**, *16*, 27.
[19] W. Zhou, M. Dridi, J. Y. Suh, C. H. Kim, D. T. Co, M. R. Wasielewski, G. C. Schatz, T. W. Odom, *Nat. Nanotechnol.* **2013**, *8*, 506.
[20] F. Van Beijnum, P. J. Van Veldhoven, E. J. Geluk, M. J. A. De Dood, G. W. 'T Hooft, M. P. Van Exter, *Phys. Rev. Lett.* **2013**, *110*, 206802.
[21] S. Pourjamal, T. K. Hakala, M. Nečada, F. Freire-Fernández, M. Kataja, H. Rekola, J. P. Martikainen, P. Törmä, S. Van Dijken, *ACS Nano* **2019**, *13*, 5686.
[22] M. S. Bin-Alam, O. Reshef, Y. Mamchur, M. Z. Alam, G. Carlow, J. Upham, B. T. Sullivan, J. M. Ménard, M. J. Huttunen, R. W. Boyd, K. Dolgaleva, *Nat. Commun.* **2021**, *12*, https://doi.org/10.1038/s41467-021-21196-2.
[23] Q. Le-Van, E. Zoethout, E. J. Geluk, M. Ramezani, M. Berghuis, J. G. Rivas, *Adv. Opt. Mater.* **2019**, *7*, 1801451.
[24] R. Hatsuoka, K. Yamasaki, K. Wada, T. Matsuyama, K. Okamoto, *Nanomaterials* **2024**, *14*, 1559.
[25] D. Dey, G. C. Schatz, *M.R.S. Bull* **2024**, *49*, 421.
[26] X. Wang, H. Lu, B. Wang, M. Liu, G. Guo, S. Ma, J. Lv, J. Liang, W. Wang, *Opt. Laser Technol.* **2025**, *185*, 112581.
[27] M. Mayer, M. J. Schnepf, T. A. F. König, A. Fery, *Adv. Opt. Mater.* **2019**, *7*, 1800564.
[28] S. Ni, L. Isa, H. Wolf, *Soft Matter* **2018**, *14*, 2978.
[29] S. Ni, H. Wolf, L. Isa, *Langmuir* **2018**, *34*, 2481.
[30] C. Hanske, M. Tebbe, C. Kuttner, V. Bieber, V. V. Tsukruk, M. Chanana, T. A. F. König, A. Fery, *Nano Lett.* **2014**, *14*, 6863.
[31] G. R. Souza, C. S. Levin, A. Hajitou, R. Pasqualini, W. Arap, J. H. Miller, *Anal. Chem.* **2006**, *78*, 6232.
[32] J. Wang, L. Yang, S. Boriskina, B. Yan, B. M. Reinhard, *Anal. Chem.* **2011**, *83*, 2243.
[33] A. Cerf, B. R. Cipriany, J. J. Benítez, H. G. Craighead, *Anal. Chem.* **2011**, *83*, 8073.
[34] A. Cerf, T. Alava, R. A. Barton, H. G. Craighead, *Nano Lett.* **2011**, *11*, 4232.
[35] A. Cerf, H. C. Tian, H. G. Craighead, *ACS Nano* **2012**, *6*, 7928.
[36] J. Cordeiro, F. Funfschilling, O. Lecarme, G. O. Dias, E. Picard, D. Peyrade, *Microelectron. Eng.* **2013**, *110*, 414.
[37] S. C. Malek, H. S. Ee, R. Agarwal, *Nano Lett.* **2017**, *17*, 3641.
[38] C. Zhang, J. Jing, Y. Wu, Y. Fan, W. Yang, S. Wang, Q. Song, S. Xiao, *ACS Nano* **2020**, *14*, 1418.
[39] I. M. Pryce, K. Aydin, Y. A. Kelaita, R. M. Briggs, H. A. Atwater, *Nano Lett.* **2010**, *10*, 4222.
[40] Y. Cui, J. Zhou, V. A. Tamma, W. Park, *ACS Nano* **2012**, *6*, 2385.
[41] K. Agata, S. Murai, K. Tanaka, *Appl. Phys. Lett.* **2021**, *118*, 021110.
[42] V. Gupta, P. T. Probst, F. R. Goßler, A. M. Steiner, J. Schubert, Y. Brasse, T. A. F. König, A. Fery, *ACS Appl. Mater. Interfaces* **2019**, *11*, 28189.
[43] V. G. Kravets, A. V. Kabashin, W. L. Barnes, A. N. Grigorenko, *Chem. Rev.* **2018**, *118*, 5912.

[44] R. Kolkowski, A. F. Koenderink, *IEEE 2020 108*, 795.
[45] M. B. Ross, C. A. Mirkin, G. C. Schatz, *J. Phys. Chem. C* **2016**, *120*, 816.
[46] B. B. Rajeeva, L. Lin, Y. Zheng, *Nano Res.* **2018**, *11*, 4423.
[47] A. I. Kuznetsov, A. E. Miroshnichenko, M. L. Brongersma, Y. S. Kivshar, B. Luk'yanchuk, *Science* **2016**, *354*, 6314.
[48] G. Mie, *Ann. Phys.* **1908**, *330*, 377.
[49] A. I. Kuznetsov, A. E. Miroshnichenko, Y. H. Fu, J. Zhang, B. Lukyanchukl, *Sci. Rep* **2012**, *2*, https://doi.org/10.1038/srep00492.
[50] A. B. Evlyukhin, S. M. Novikov, U. Zywietz, R. L. Eriksen, C. Reinhardt, S. I. Bozhevolnyi, B. N. Chichkov, *Nano Lett.* **2012**, *12*, 3749.
[51] Y. H. Fu, A. I. Kuznetsov, A. E. Miroshnichenko, Y. F. Yu, B. Luk'yanchuk, *Nat. Commun.* **2013**, *4*, https://doi.org/10.1038/ncomms2538.
[52] V. E. Babicheva, A. B. Evlyukhin, *ACS Photonics* **2018**, *5*, 2022.
[53] Y. L. Tang, T. H. Yen, K. Nishida, C. H. Li, Y. C. Chen, T. Zhang, C. K. Pai, K. P. Chen, X. Li, J. Takahara, S. W. Chu, *Nat. Commun.* **2023**, *14*, 7213.
[54] N. A. Butakov, J. A. Schuller, *Sci. Rep.* **2016**, *6*, https://doi.org/10.1038/srep38487.
[55] A. B. Evlyukhin, C. Reinhardt, A. Seidel, B. S. Luk'Yanchuk, B. N. Chichkov, *Phys. Rev. B – Condens. Matter Mater. Phys.* **2010**, *82*, 045404.
[56] V. E. Babicheva, A. B. Evlyukhin, *Laser Photon. Rev.* **2017**, *11*, https://doi.org/10.1002/lpor.201700132.
[57] L. Liu, F. Zhang, S. Murai, K. Tanaka, *Adv. Photonics Res.* **2022**, *3*, 2100235.
[58] R. Paniagua-Domínguez, Y. F. Yu, A. E. Miroshnichenko, L. A. Krivitsky, Y. H. Fu, V. Valuckas, L. Gonzaga, Y. T. Toh, A. Y. S. Kay, B. Lukyanchuk, A. I. Kuznetsov, *Nat. Commun.* **2016**, *7*, 10362.
[59] L. Xiong, X. Zhao, X. Du, S. Chen, Y. Lu, H. Ding, G. Li, *Nano Res.* **2023**, *16*, 3195.
[60] P. D. Terekhov, V. E. Babicheva, K. V. Baryshnikova, A. S. Shalin, A. Karabchevsky, A. B. Evlyukhin, *Phys. Rev. B* **2019**, *99*, 045424.
[61] H. Sugimoto, T. Okazaki, M. Fujii, *Adv. Opt. Mater.* **2020**, *8*, 2000033.
[62] E. D. Palik, *Handbook of Optical Constants of Solids*, Academic Press, Cambridge, Massachusetts **1998**.